Joule

CellPress

Article

High-Energy Li Metal Battery with Lithiated Host

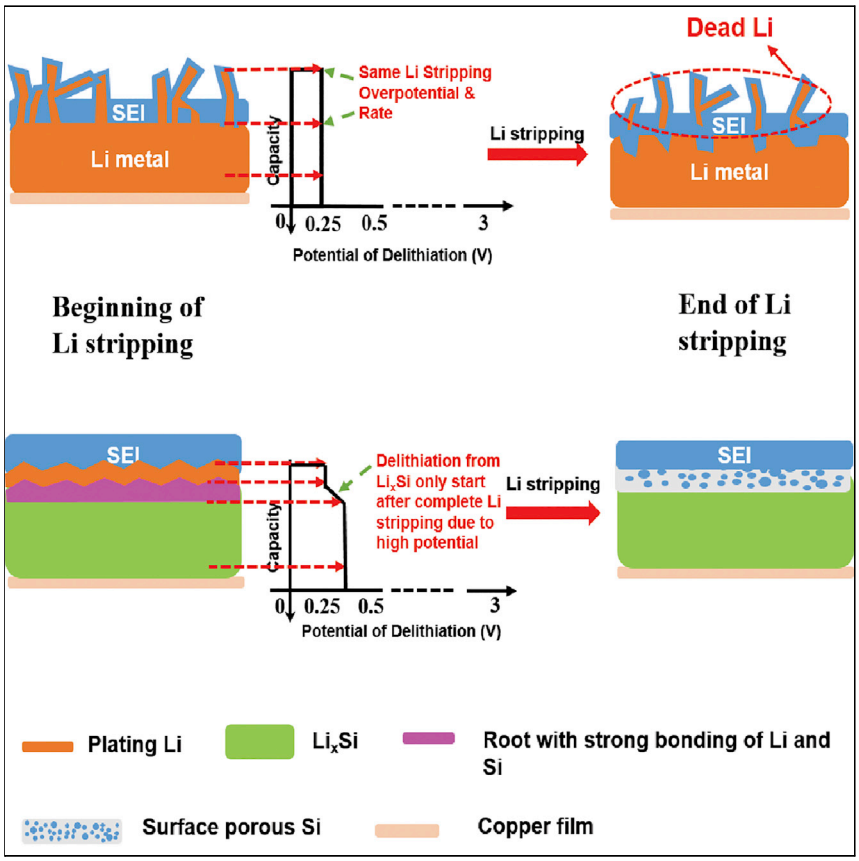

Lithiated silicon significantly increases the Li plating/stripping Coulombic efficiency to a recorded highest value of >99.7% due to successful elimination of the dead Li. The reported principle can be broadly applied to other active materials (such as Sn, Bi, Sb) for other metal anodes including K and Na batteries. The discovery opens up an entirely new avenue for all alkali metal batteries and will attract a broad range of scientists and engineers working on metal anode battery technologies in general.

Long Chen, Xiulin Fan, Xiao Ji, Ji Chen, Singyuk Hou, Chunsheng Wang

cswang@umd.edu

HIGHLIGHTS

Lithiated Si host enables a Li plating/stripping Coulombic efficiency of >99.7%

No formation of dead Li

NMC 811/Li_xSi cell (energy density 600 Wh/kg) retains 90% capacity after 300 cycles

Chen et al., Joule 3, 732–744
March 20, 2019
https://doi.org/10.1016/j.joule.2018.11.025

Joule

CellPress

Article

High-Energy Li Metal Battery with Lithiated Host

Long Chen,[1,2] Xiulin Fan,[1,2] Xiao Ji,[1,2] Ji Chen,[1] Singyuk Hou,[1] and Chunsheng Wang[1,3,*]

SUMMARY

Lithium metal batteries (LMB) are promising energy storage systems due to the highest capacity of Li (3,860 mAh/g). However, the low Coulombic efficiency of Li plating/stripping and safety concern due to uncontrolled Li dendrite and dead Li prevent its applications. Here, we report that Li plating on a prelithiated Li_xSi anode can effectively suppress the formation of dead Li on Li_xSi when the total lithiation/delithiation capacity in each cycle is higher than the Li plating/stripping capacity on Li_xSi because the slight delithiation from Li_xSi at a higher delithiation potential than the stripping potential of deposited Li on Li_xSi will ensure the complete stripping of the plated Li before delithiation of Li_xSi, the root of deposited Li, thus dramatically enhancing the Coulombic efficiency of Li plating/stripping to the highest recorded (>99.7%) even at a high Li plating/stripping capacity of 1.0 mAh cm^{-2}.

INTRODUCTION

Advances in lithium ion batteries has significantly changed our daily life. The recent booming market for electric vehicles requires Li-ion batteries to have a higher energy density of ~500 Wh/kg to compete with conventional gas engine-powered vehicles. However, it is very challenging for current Li-ion chemistry to reach a goal of 500 Wh/kg[1–3] due to the limited capacity of intercalation graphite anodes and transition metal cathodes. Li metal has the highest specific capacity (3,860 mAh/g) and lowest operation potential (−3.04 V versus standard hydrogen electrode), so the Li metal battery (LMB) becomes the ultimate choice for electric vehicle batteries.[3–5] However, Li will intensely react with electrolytes forming a non-uniform solid electrolyte interphase (SEI), promoting the growth of dendrite Li and formation of dead Li during Li plating/stripping cycles at a high cycling capacity (>2 mAh cm^{-2}), significantly reducing the Coulombic efficiency (CE) of the Li metal anode to a very low level of <90% in traditional carbonate electrolytes.[6–8] The formation of dendrite Li and dead Li potentially cause short circuiting of batteries, with serious safety issues.[9–14] The "dead Li" is formed by Li stripping from the roots of Li dendrite metal, which breaks the electrical contact to the substrate because the stripping potential at the root of the Li dendrite is the same as the stripping potential at the top of the Li dendrite (Figure 1A). After continuous cycling, the Li metal anode will be covered by a thick accumulated SEI layer and dead Li composite, which blocks Li-ion transport and leads to exponential increase of resistance and cell failure.[4,15] To offset the low CE of the Li metal due to the continuous growth of SEI and the continuous formation of dead Li, plenty of excess Li metal has to be paired with the cathodes, which dramatically reduces the energy density of the full LMBs.

To suppress the Li dendrite and dead Li, 3D or porous host with large surface area including hollow carbon spheres,[6] layered reduced graphene oxide,[16] hollow

Context & Scale

As Li metal has the highest specific capacity (3,860 mAh/g) and lowest operation potential (−3.04 V), the Li metal battery becomes the ultimate choice for electric vehicle batteries. However, the Coulombic efficiency (CE) of Li plating/stripping in non-aqueous electrolytes is only <99.2% due to uncontrolled Li dendrite and dead Li, which also potentially cause serious safety issues. In the present work, we conceive a new concept that use of a Si alloy host that not only allows Li to uniformly plate on the host surface with strong root due to a strong bonding to Li but also has the ability to avoid the formation of "dead" Li due to a higher delithiation potential than a Li stripping potential results in an extremely high Li plating/stripping CE of 99.7% at 2 mAh/cm^2. The high capacity of the Si host can compensate capacity loss due to 98% CE of Li plating/stripping, a shallow delithiation/lithiation of Si ensuring a long cycle life.

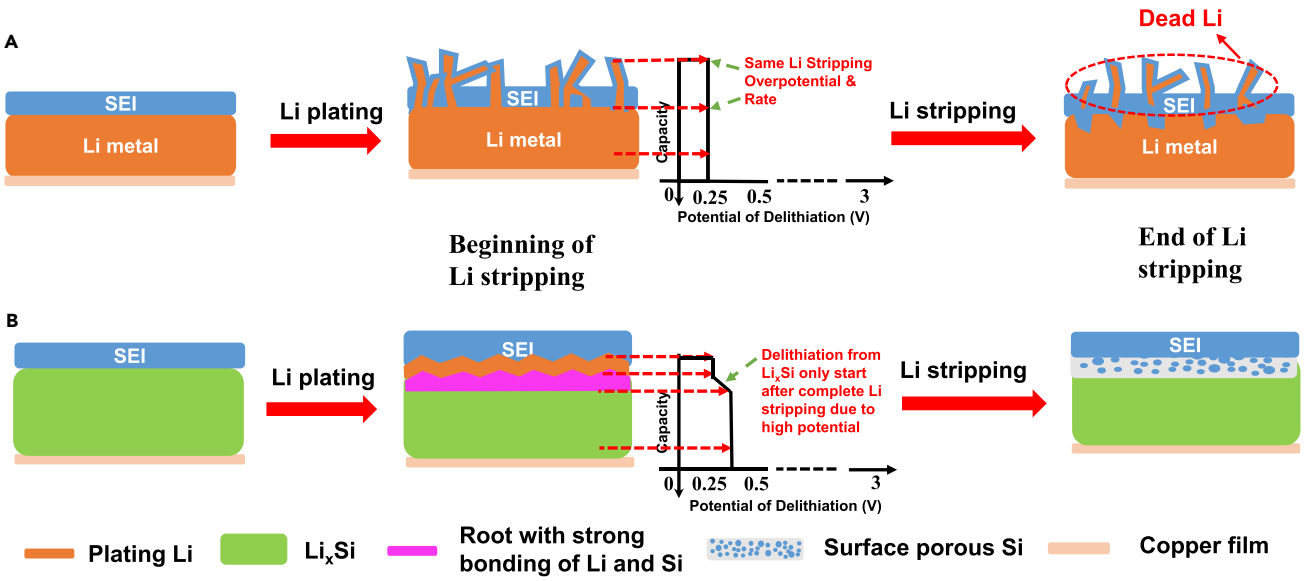

Figure 1. Schematic Diagrams of Different Li Metal Anode Host Structures

(A) A thin film of the SEI layer (blue) forms on the surface Li metal (golden). Volumetric changes of deposited Li during the plating process can easily break the SEI layer. "Dead Li" formed due to Li stripping from the roots.

(B) A thin film of the SEI layer forms on the surface of the prelithiated Si (Li_xSi) electrode, Li depositing on the surface of Li_xSi with a root which has strong bonding of Li with Si, and stripping entirely before the delithiation of Li_xSi because of the potential difference. A few Li-ions extract from the host (Li_xSi) to form surface porous Si during the discharging process.

carbon with golden seeds,[17] hollow carbon fibers,[18] graphene nanoribbons,[19] polymeric matrix,[20] 3D porous carbon matrix,[21] and copper nanowire networks,[22] were used to reduce the actual cycling current. Although the Li dendrite has been suppressed at a low actual current, the high interface area with electrolytes of 3D and porous host also increase the amount of SEI, which significantly reduces the CE, especially in the first few cycles. Since the delithiation potential of these porous carbonous hosts is similar to the Li stripping potential, especially at a high stripping current, and that these inactive 3D current collectors have weak bonding to Li, Li can still be stripped from the roots of Li metal during the Li stripping process, resulting in dead Li similar to the Li metal shown in Figure 1A. Therefore, the CEs of the Li metal plating-stripping in these hosts are still much lower.[4,16–22]

An effective host should not only allow Li to uniformly plate on the host surface, but also have the ability to avoid the formation of dead Li. The ideal host should satisfy the following requirements: (1) the substrate should be an active material with a strong bonding to Li for uniform Li plating, and the delithiation potential (~0.3 V) of the host should be slightly higher than that of the Li stripping potential (0.25 V depending current) to ensure that Li on the surface of host (root of Li dendrite) does not deplete until complete stripping of deposited Li on the top. The delithiation potential of the host should also not be too high, which would decrease the average voltage and reduce the energy density of the full cell, such as Sn (>0.5 V).[23] (2) It should have high capacity and be structurally stable during shallow delithiation/lithiation cycles. Since the CE of Li plating/stripping cannot reach 100%, the host experiences a very shallow delithiation/lithiation process during each Li plating/stripping cycle. If dead Li can be avoided and SEI on plated Li is stable, the CE of Li plating/stripping on the host should be the same as the CE of the host during the very shallow delithiation/lithiation cycles, representing a revolutionary increase for Li metal anode.

[1]Department of Chemical and Biomolecular Engineering, University of Maryland, College Park, MD 20742, USA

[2]These authors contributed equally

[3]Lead Contact

*Correspondence: cswang@umd.edu

https://doi.org/10.1016/j.joule.2018.11.025

Here, we use silicon as a model electrode to demonstrate such an innovative concept. Si is an ideal model anode for Li plating/stripping because: (1) Si has a strong bonding with Li and has a suitable delithiation potential of 0.3 V (depending on current density and the material used in this work, Figure 3A). The stronger preferential adsorption of Li-ions onto the Si atom rather than the Li atom can induce a uniform Li deposition and result in smaller nucleation over-potential for Li plating, which has been demonstrated in a pioneering study by simply coating a Si nano-layer on the Li anode.[24] The strong bonding with Li and the suitable delithiation potential of 0.3 V of Si can prevent Li stripping from the roots during the stripping process, which results in the formation of dead Li (Figure 1B); However *in-situ*-coated Sn[25] or *ex-situ*-coated Si[24] nano-layers on the Li foil anode have the same potential as Li during Li stripping, so they cannot prevent dead Li. In addition, the repeat Li plating/stripping on Si- or Sn-coated Li may break the Si or Sn nano-layer allowing the liquid electrolyte to penetrate underneath Li, forming Li dendrites and dead Li, and reducing the CE. (2) The high capacity (>3,000 mAh/g) of Si[26–28] can effectively accommodate the Li loss ensuring long cycle life, and the repeated shallow delithiation/lithiation of Li_xSi can generate nano-pores on the Li_xSi surface that increase the surface area (Figure 1B), which can reduce the effective current density and minimize the volume change of deposited Li. By coupling the $LiNi_{0.8}Mn_{0.1}Co_{0.1}O_2$ (NMC 811) cathode with the lithiated silicon (Li_xSi) electrode at a capacity ratio of NMC 811 to Li_xSi of 1:1, and using 1 M $LiPF_6$ in all-fluorinated solvent as an electrolyte (1 M $LiPF_6$ in fluoroethylene carbonate (FEC)/bis(2,2,2-trifluoroethyl) carbonate (FDEC)/hydrofluoroether (HFE) [2:6:2 by volume]), we demonstrated that the Li_xSi/NMC 811 full cell provided an energy density of 600 Wh/kg (of total mass of cathode and anode) at a high areal capacity of 2.0 mAh cm^{-2} and maintained 90% of initial energy density after 300 cycles. The average CE of Li_xSi anode back calculated from the capacity decay of Li_xSi/NMC 811 full cell after 300 cycles is >99.7%, as the CE of NMC 811 is >99.9% in 300 cycles. The CE for Li plating/stripping on the Li_xSi host is similar to that of the Si anode, and is much higher than the CE of Li anode (<99%) in the same electrolyte. The much longer cycle life (>300) of Li_xSi/NMC 811 with a capacity ratio (Li_xSi to NMC 811) of 1.0 than that (220) of Li/NMC 811, with a capacity ratio (Li to NMC 811) of 10.0, and that (40) of Si/NMC 811 with the same amount of Si loading as in Li_xSi/NMC 811, demonstrated the significant advantages of a lithiated Si host for Li plating/stripping.

RESULTS AND DISCUSSION

FEC-containing electrolytes have a high stability to Li and Si anodes and the high-voltage NMC 811 cathode.[29,30] To further enhance the stability of the electrolyte, we increased the fluorine content by adding large amounts of two other fluorinated solvents forming 1 M $LiPF_6$ in FEC/FDEC/HFE (2:6:2, by volume, see Experimental Procedures for details), which enables the CE for Li plating/stripping metal to achieve 99% at a current density of 0.5 mA cm^{-2} (Figures S1A and S1B) and a small over-potential, which is in agreement with a reported all-fluorinated electrolyte.[30] The X-ray photoelectron spectroscopy (XPS) results (Figures S1C–S1G) demonstrated that the lithium fluoride (LiF) content in SEI is higher than >80%. The extremely low electronic conductivity[31] and high interfacial energy of LiF to Li metal[32] enable a successful 200 cycles of the Li metal anode at a current of 0.5 mA cm^{-2} in this all-fluorinated electrolyte. However, when the current density is increased to 4 mA cm^{-2}, the cycle stability of the Li metal anode decreases dramatically. Figure 2A shows the voltage profile for galvanostatic lithium plating/stripping on a symmetric lithium metal cell at a current density of 4 mA cm^{-2}, with a cycling capacity of 0.5 mAh cm^{-2}. The over-potential for lithium plating and

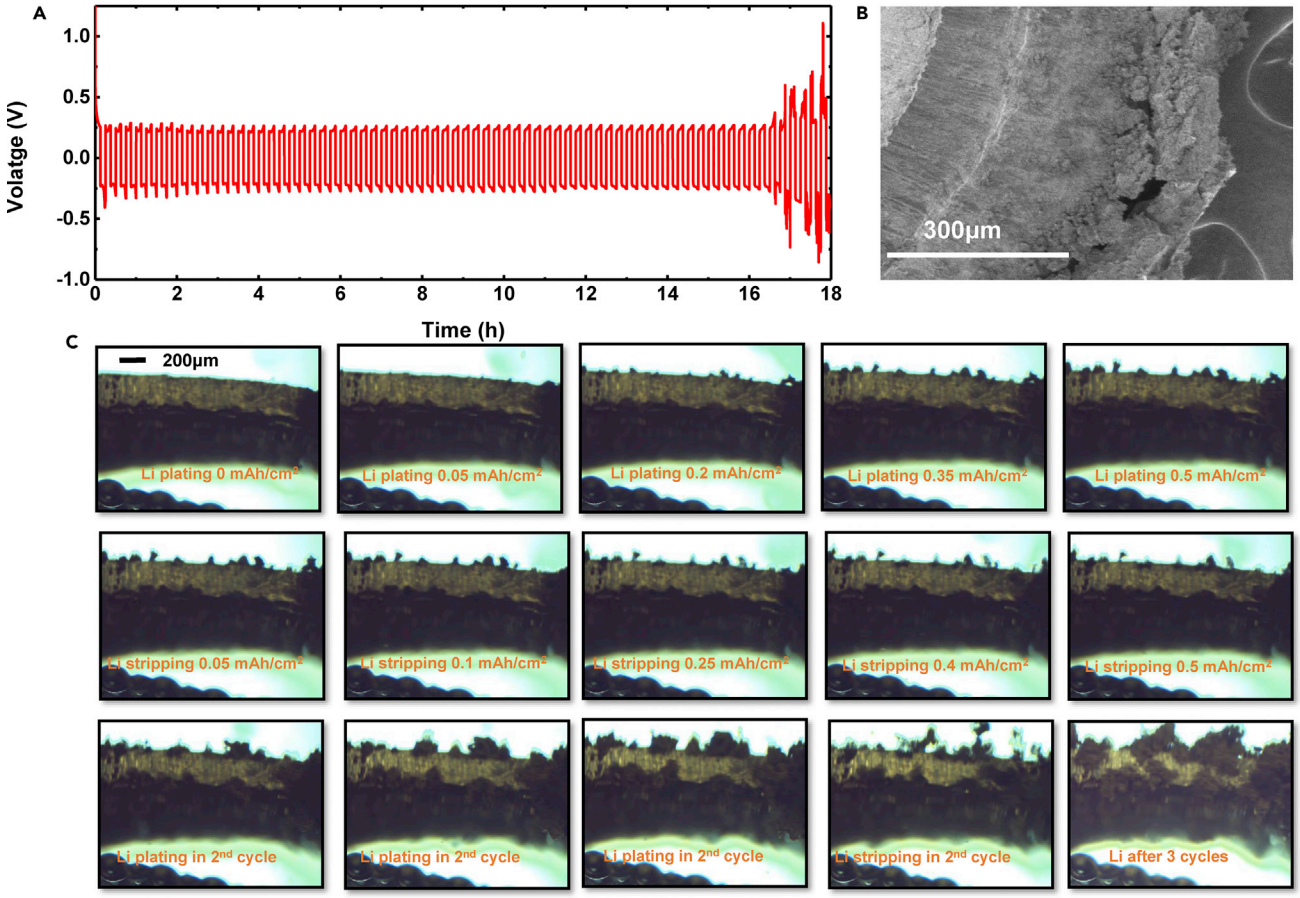

Figure 2. Electrochemical Performance of Li Metal Anode and Optical Microscopy Images of the Li Metal Anode Surface

(A) Voltage profile for galvanostatic lithium plating/stripping on the symmetric lithium metal cell at a current density of 4 mA cm^{-2} for 0.5 mAh at each step.

(B) Scanning electron microscope (SEM) image of the Li metal anode surface after the experiment in (A) for 18 hr.

(C) Capacity-sequenced optical microscopy images of the electrolyte-electrode interface during Li plating and stripping on lithium metal anode at a current density of 4 mA cm^{-2}. The capacity (mAh cm^{-2}) of lithium being plated or stripped on the Li metal anode is shown in the middle of each image.

stripping suddenly increased from approximately 250 mV to more than 500 mV after 16.5 hr of galvanostatic lithium plating/stripping. The scanning electron microscope (SEM) image of this Li metal at 18 hr of stripping/plating shows a highly porous and thick dead Li layer on the Li metal substrate (Figure 2B), which seriously blocked Li-ion transport and dramatically increased the over-potential of Li plating and stripping. To clearly reveal the formation process of dead Li during Li plating and stripping on the Li metal anode at a high current, an optical microscope was applied to visualize the Li plating/stripping process using a custom-built optical cell. The time-lapse images of the morphology at the electrolyte/Li metal interface during Li plating and stripping at a current density of 4 mA cm^{-2} are shown in Figure 2C. The fresh Li metal anode has a smooth morphology. After 0.5 mAh cm^{-2} of electrochemical Li deposition, a few mound-like Li grow on the Li substrate. These mound-like plated Li shrank during the Li stripping, but did not disappear even after 0.5 mAh cm^{-2} of stripping. As schematically demonstrated in Figure 1A, the Li strips not only from the top surface of plated Li but also from the roots, forming dead Li. In the subsequent plating process, rapid and uncontrollable mossy deposited Li were observed on the Li metal electrode. Video S1 shows the formation/growth of Li

dendrites and dead Li in several Li plating and stripping cycles. As expected, many dead Li, of several microns, were peeled off from the Li metal electrode during the stripping process. Since these dead Li electrically disconnected with the Li metal electrode but physically connect with the Li electrode by weak SEI, they also peeled off in the plating process due to the volume expansion the plated Li.

The electrochemical Li plating and stripping on the lithiated silicon (Li_xSi) substrate was also investigated. Firstly, the electrochemical performance of silicon anodes was evaluated in the all-fluorinated electrolyte. At a current density of 0.5 mA cm^{-2}, the reversible Li extraction specific capacity of the Si anode at a potential range of 1.5–0.05 V is 1,083 mAh g^{-1} (the area capacity is ~2.2 mAh cm^{-2}) (Figure 3A), and the Si still maintains 75% of initial capacity after 300 cycles (Figure 3B). The CE of the Si in the first cycle is 90% and rapidly increases to 99.8% after 10 cycles (Figure 3C). The XPS results indicated that the content of LiF in SEI on Si is also extremely high, which enables the high CE and cycling stability of Si anode in the fluorinated electrolytes (Figures S2 and 3). The benefit of LiF-rich SEI for Si anodes have been confirmed in previous studies.[33,34]

Figure 3D shows the electrochemical Li plating and stripping process on the lithiated silicon (Li_xSi) host. An Li_xSi host with a lithiation capacity of 2.2 mAh cm^{-2} was achieved in the same all-fluorinated electrolyte by galvanostatic discharging a Li||Si half-cell to a cutoff voltage of 0.005 V at a current density of 0.5 mA cm^{-2} (Figure 3D, blue). Then an additional lithiation of 2.0 mAh cm^{-2} was applied to lithiated Si to deposit Li metal on Li_xSi (Figure 3D, golden). As demonstrated in the expended lithiation potential profile in Figure 3E, Li plating on Li_xSi begins after discharging of Si to 3.1 mAh cm^{-2} at −0.065 V where a clear Li nucleation over-potential is observed. After Li plating on Li_xSi for a capacity of 1.1 mAh cm^{-2}, the lithiation process is finished. During the delithiation (charged) process, plated Li on the Li_xSi surface is first stripped, followed by a shallow delithiation of the Li_xSi because of the higher delithiation potential of Li_xSi than the stripping potential of the plated Li metal (Figure 3D, red).

An optical microscope was also used to capture time-lapse images of the interface between the electrolyte and the silicon electrode during the lithiation of Si following Li plating on the surface of the Li_xSi electrode. Time-lapse images in the delithiation process (charging process) were also recorded. Figure 3F and Video S2 show the evolution of the Si surface during the complete 4.2 mAh cm^{-2} lithiation process (including 3.1 mAh cm^{-2} Li-ions lithiating into Si and 1.1 mAh cm^{-2} Li metal plating on the surface of the silicon electrode) and 2 mAh cm^{-2} of delithiation process at a current density of 0.5 mA cm^{-2}. During the initial lithiation of Si to 2.0 mAh cm^{-2}, the Si electrode experiences an obvious thickness increase from 314 to 457 μm due to volume expansion. Upon further lithiation of Li_xSi from 2.0 to 3.0 mAh cm^{-2}, the thickness of Li_xSi further increases only by 6% from 457 to 488 μm (Figure 3F). The 6% of volume change in the limited lithiation of Si with 1.0 mAh cm^{-2} is similar to the volume change of $LiFePO_4$, which is one of the most stable cathodes in Li-ion batteries. The thickness of the electrode further increases to 528 μm in the subsequent Li metal plating process from 3.0 to 4.0 mAh cm^{-2} (Figure 3F). As expected, no dendrite or mound-like plated Li metal is observed during Li plating on lithiated Si. In addition, SEM images of lithiated Si at the end of Li plating process also showed no obvious dendrite Li metal on the surface (Figure 4). During the subsequent delithiation process to 2 mAh cm^{-2}, no dead Li exfoliation can be observed from the Li_xSi electrode (Figure 3F, delithiation from 0.25 to 2 mAh cm^{-2}, Video S2). Accordingly, the thickness of the electrode decreases from 528 to 456 μm

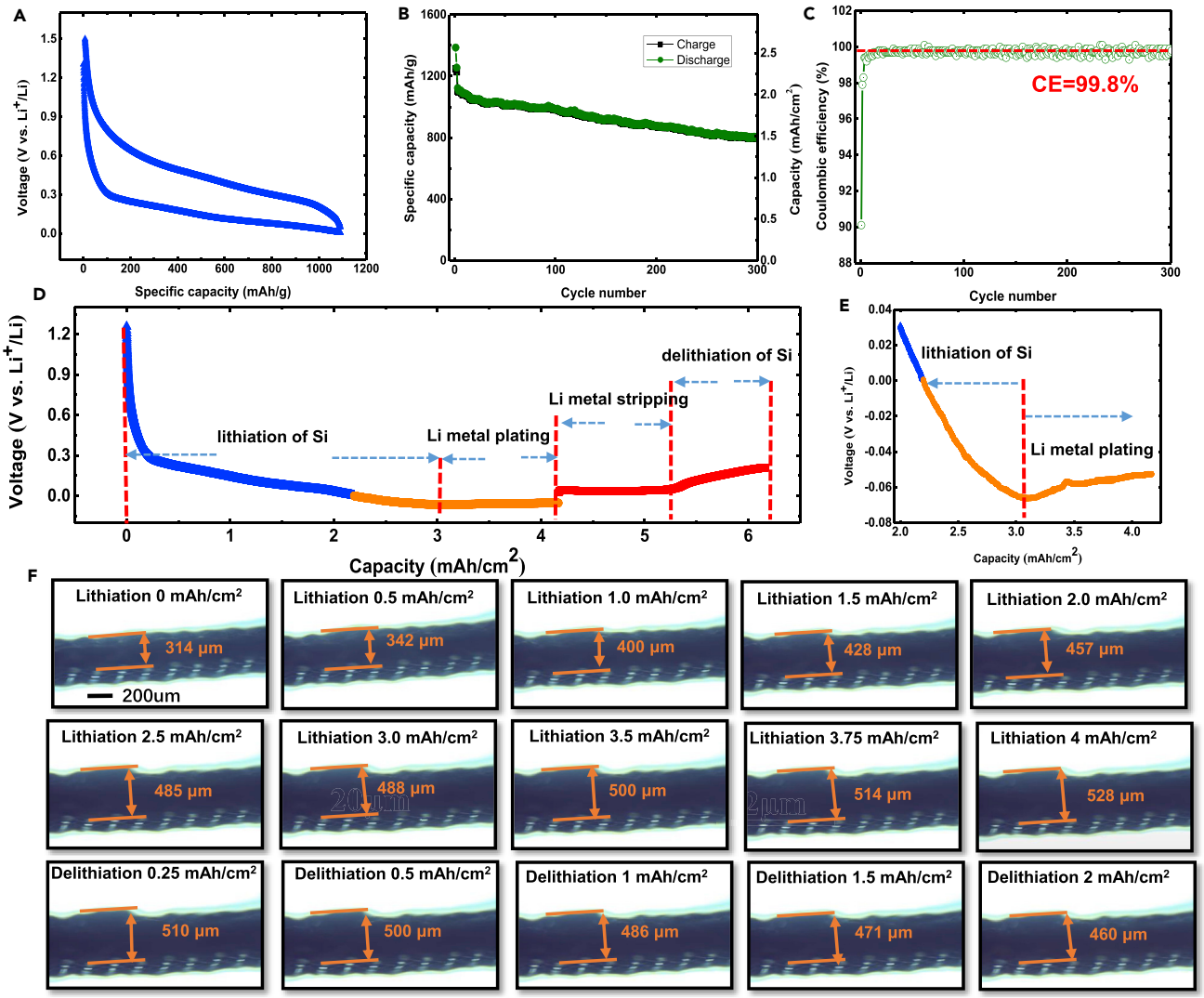

Figure 3. Electrochemical Profiles of the Silicon Anode and Li Plating/Stripping on the Li_xSi Electrode

(A) Galvanostatic charge-discharge profile of the silicon electrode cycled at a current density of 0.5 mA cm^{-2} between 0.005 and 1.5 V (versus Li^+/Li).

(B) Cycle performance of the silicon electrode at a current density of 0.5 mA cm^{-2} (the current density is 0.1 mA cm^{-2} during the first 3 cycles).

(C) Coulombic efficiency (CE) of the silicon electrode at a current density of 0.5 mA cm^{-2}.

(D) Voltage profile of the Si electrode discharged to 0.005 V at a current of 0.5 mA cm^{-2} (blue), voltage profile of continued discharging process with a capacity of 2 mAh at a current of 0.5 mA cm^{-2} (golden), voltage profile of charging process with a capacity of 2 mAh at the current of 0.5 mA cm^{-2} (red).

(E) Detailed voltage profile of lithium plating on the Li_xSi electrode host.

(F) Capacity-sequenced optical microscopy images of the electrolyte-electrode interface during the lithiation (4 mAh cm^{-2}) and delithiation processes (2 mAh cm^{-2}) on the Si electrode at a current density of 0.5 mA cm^{-2}. The capacity (mAh cm^{-2}) of lithiation and delithiation on the Si electrode is shown in the middle of each image.

during the stripping of deposited Li and shallow delithiation of Li_xSi, demonstrating high reversibility in the thickness.

First principles and molecular dynamic (MD) calculations were applied to reveal the mechanism for the suppressing the formation of Li dendrites and dead Li. Figure 5 illustrates Li-ion plating and stripping behavior on the lithiated silicon surface. Firstly, Si-Li bonding is stronger than Li-Li bonding, suppressing the Li stripping from the interface between Si and Li (at the root of deposited Li). The first-principles calculation demonstrated that the binding energies of Li on Si-doped Li(001) and

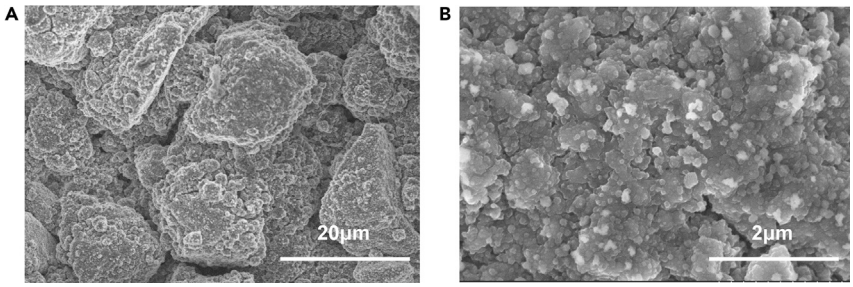

Figure 4. SEM Images of the Li Plating on the Li_xSi Host
SEM images at the end of Li plating process (at the end of the golden profile in Figure 3D).

Li(001) surfaces are calculated to be −1.60 and −0.55 eV, respectively (Figures 5A and 5B). The more than 1.0 eV lower binding energy indicates a stronger preferential adsorption of Li-ions onto the Si atom rather than the Li atom. The charge density calculation suggests the Si atom owing the stronger electron localization ability than Li, which suggests that the electron prefers to accumulate at the Si atoms when it is charged by the electrons. According to the voltage profiles, the lithiation of Si will take place before Li plating, forming $Li_{3.75\pm w}Si$ (Figure 5C).[35] The higher voltage of the Li-Si alloy also suggests a stronger interaction between Li and Si atoms. Moreover, the average Si-Si pairs in $Li_{3.75\pm w}Si$ are calculated to be ~2.5 Å according to the pair distribution function (PDF) and the coordination number of Si-Si to range from 1.0 to 2.0 (see Figure S4). These results indicate that Si atoms uniformly disperse in the $Li_{3.75\pm w}Si$ alloy in 3D. The Monte Carlo simulations shown in Figures 5D and 5E manifest that Si atoms in the Li-Si alloy provide dispersive seeds for Li nucleation. As schematically illustrated in Figure 5F, while discharging, Li-ions migrate toward the anode surface under the dual effect of the electric field and concentration gradient, and insert Si, forming an Li-Si alloy. After lithiation into the Si process, Li plating begins at the surface of the Li-Si alloy. The dispersed lithiophilic Si atoms offer nucleation sites, induce a uniform Li deposition, and result in smaller nucleation over-potential for Li plating. In the following growth stage, Li uniform nucleation acts as a Li plating matrix, significantly improving both the plating process and final morphology. When complete, the surface of the Li-Si alloy will be covered with uniform and smooth Li deposits. During the subsequent Li stripping process, the stronger preferential adsorption of Li-ions on the Si atom rather than the Li atom prevent Li stripping from the roots, which suppresses the formation of dead Li.

During 2 mAh cm^{-2} of charge/discharge cycles, the Li_xSi anode experiences a shallow delithiation/lithiation process (1.0 mAh cm^{-2}) with a volume change of 6%. The shallow charge/discharge cycles ensure a high CE and the formation of a porous structure. Transmission electron microscope (TEM) images of the silicon after one Li plating and stripping cycle show that a large amount of pores and slits are formed on the surface layer of the Si particle (Figure S5), which enhances the bonding to Li and further suppressing Li stripping from the interface between Si and Li (root of deposited Li). The porous Si also minimizes the volume change of lithiated Si and subsequent deposition of Li metal, which enhances the CE.

For comparison, we used a 2.0 mAh cm^{-2} NMC 811 cathode to match with three anodes: a Li metal anode with 10-fold excess capacity (20 mAh cm^{-2}), a Si anode (2.0 mAh cm^{-2}), and a prelithiated Li_xSi anode (2.0 mAh cm^{-2}) (the same amount of Si) (Figure 6). The NMC 811 cathode delivered a specific capacity of

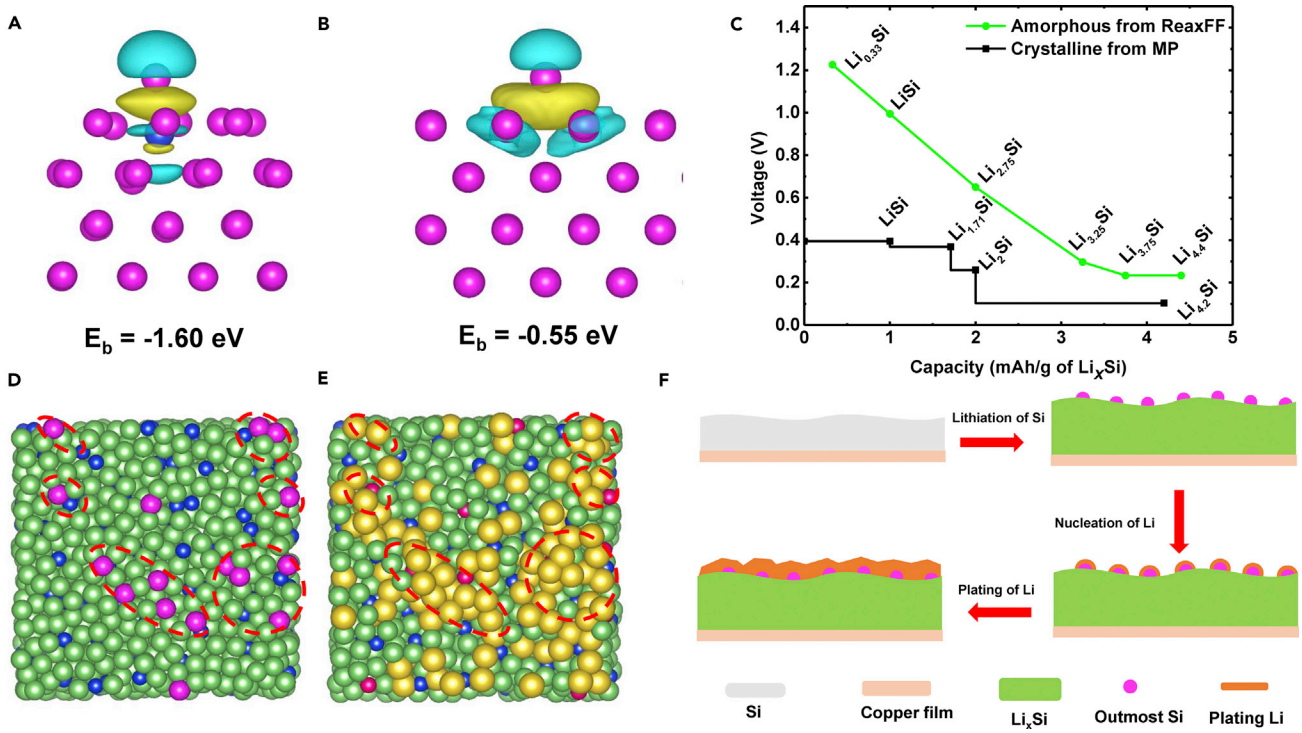

Figure 5. First-Principles and Molecular Dynamic Calculations to Illustrate Li-Ion Plating and Stripping Behaviors on the Li-Si Alloy Surface

(A and B) Differences of charge density for Li on (A) Si-doped Li (001) and (B) Li (001) surfaces and their corresponding binding energies. The turquoise and yellow regions represent the deletion and accumulation of electrons, respectively.

(C–E) The calculated voltage profiles for amorphous Li-Si alloy form ReaxFF force field and crystalline Li-Si alloy form materials project (MP) (C). Illustration of atomic structure of $Li_{3.75\pm w}Si$ surface (D) before and (E) after Li platting. The green and blue balls represent the Li and Si atoms in the substrate, while the yellow and purple balls represent the platted Li and outmost Si atoms.

(F) Schematic representation of the Li nucleation and plating process on Si electrode.

200 mAh g^{-1} (Figure S6), with a high area capacity of ~2 mAh cm^{-2}; such a high cathode loading presents a rigorous test for the cycle stability for the full cell because it requires a high utilization of the anode in each cycle, which maximizes the parasitic reactions on the anode, especially for the deposited Li metal anode. The NMC 811(2 mAh)||Li metal(20 mAh) with 10-fold Li excess (~5.5 mg) delivers a stable capacity for 200 cycles with a >99.9% CE (Figures 6A, 6B, and S7A); the CE of NMC 811 is 99.99% since the Li counter electrode has a 10-fold higher capacity than NMC 811. However, the high Li amount also reduces the total capacity and energy density. The continuous reaction between Li and the electrolytes also requires high electrolyte loading, further reducing the energy density. The specific capacity of the NMC 811(2 mAh)||Li metal(20 mAh) full cell is only around 130 mAh g^{-1} and the energy density is only ~487 Wh/kg (mass of both NMC and Li). Even worse, it suffers a sudden death around 220 cycles due to the dead Li on the Li metal anode and dryness of the electrolytes (Figure S8), as discussed above in Figures 1A and 2. The SEM images of the Li anode after 240 cycles (half capacity was lost) in NMC 811(2 mAh)||Li metal(20 mAh) cell show the large thickness of the highly porous and cracked dead Li layer above the Li metal, which seriously consumed the electrolyte, blocking Li-ion transport, and leading to serious capacity fading (Figures S8A and S8B). The dead NMC 811(2 mAh)||Li metal(20 mAh) cell (after 240 cycles) was disassembled, and a new Li metal anode (20 mAh, ~5.5 mg) was used to replace the cycled Li anode. The new NMC 811(2 mAh)||Li metal(20 mAh) cell delivers a good cycle performance again (Figures S8C and S8D), which confirms that the dramatic capacity

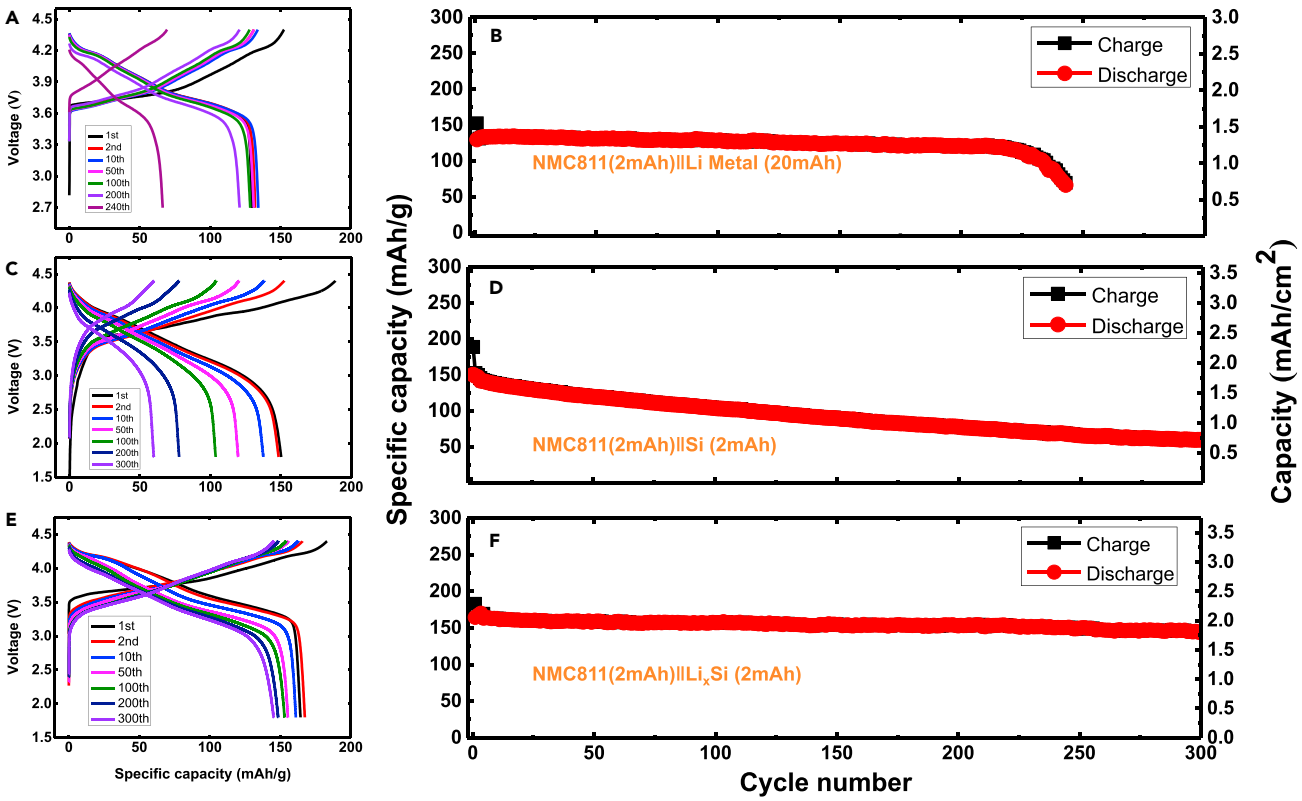

Figure 6. Electrochemical Performances of Batteries Using the NMC 811 Cathode with Different Anodes

(A) Galvanostatic charge-discharge profiles of NMC 811(2 mAh)||Li metal(20 mAh) batteries at a current density of 0.5 mA cm^{-2} between 2.7 and 4.4 V, the weight of 2 mAh NMC 811 is ~10 mg and 20 mAh Li metal is ~5.5 mg.

(B) Cycle performance of the NMC 811(2 mAh)||Li metal(20 mAh) battery at a current density of 0.5 mA cm^{-2} between 2.7 and 4.4 V.

(C) Galvanostatic charge-discharge profiles of the NMC 811(2 mAh)||Si(2 mAh) battery at a current density of 0.5 mA cm^{-2} between 1.8 and 4.4 V, the weight of 2 mAh Si is ~2 mg.

(D) Cycle performance of the NMC 811(2 mAh)||Si(2 mAh) battery at a current density of 0.5 mA cm^{-2} between 1.8 and 4.4 V.

(E) Galvanostatic charge-discharge profiles of the NMC 811(2 mAh)||Li$_x$Si(2 mAh) battery at a current density of 0.5 mA cm^{-2} between 1.8 and 4.4 V, the weight of 2 mAh Li$_x$Si is ~2.5 mg.

(F) Cycle performance of the NMC 811(2 mAh)||Li$_x$Si (2 mAh) battery at a current density of 0.5 mA cm^{-2} between 1.8 and 4.4 V.

fading was caused by the dead Li. The battery NMC 811(2 mAh)||Si(2 mAh) delivers a specific discharge capacity of 150 mAh g^{-1} (mass of NMC and Li), with a CE of only 99.8% (Figures 6C, 6D, and S7B) due to the low CE of the Si anode of 99.8% (Figure 3C), resulting in a rapid capacity decay to 60 mAh g^{-1} after 300 cycles.

As expected, the NMC 811(2 mAh)||Li$_x$Si(2 mAh) batteries showed the best cycling stability, with a capacity retention of 90% over 300 cycles and a >99.9% CE (Figures 6E, 6F, and S7C); even Li$_x$Si experiences a Li plating/stripping process during charge/discharge cycles. The achieved specific capacity is ~160 mAh g^{-1} (total mass of NMC and Li$_x$Si), and the energy density reaches ~600 Wh/kg, which is much higher than commercial Li-ion batteries and any reported Li metal batteries (including the excess Li metal anodes). According to the voltage profiles of this battery in different cycles, a gradual decrease in discharging voltage could be observed due to the gradually increased state of delithiation in Li$_x$Si during the charge/discharge cycles, complementing the Li loss in each cycle from ~99.7% of coulombic efficiency in the Li$_x$Si anode (Figure 3C). Furthermore, the NMC 811(2 mAh)||Li$_x$Si(2 mAh) cell also delivered a high performance rate, with a capacity retention

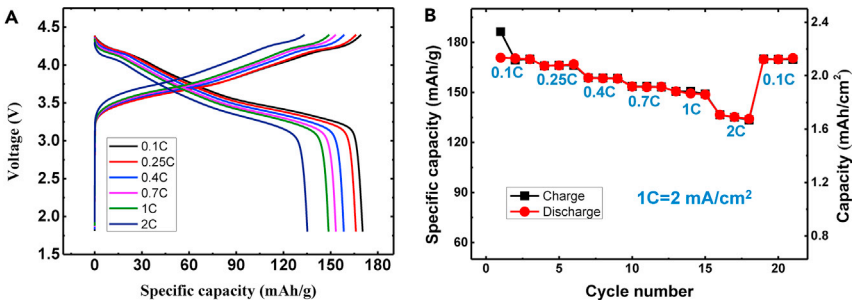

Figure 7. Rate Performance of the NMC 811(2 mAh)||Li_xSi(2 mAh) Battery

(A) Galvanostatic charge-discharge profiles of the NMC 811(2 mAh)||Li_xSi(2 mAh) battery at different current density between 1.8 and 4.4 V.

(B) Rate performances of the NMC 811(2 mAh)||Li_xSi(2 mAh) battery at different current densities between 1.8 and 4.4 V.

of 80% (135 mAh g^{-1}) at a high rate of 2C (4 mA cm^{-2}) (Figure 7). The significant enhancement in performance is mainly attributed to the Li_xSi host, with minor contributions from all-fluorinated electrolytes, as demonstrated by the better electrochemical performance of the NMC 811(2 mAh)||Li_xSi(2 mAh) cell, with only 1-fold Li excess than that of NMC 811(2 mAh)||Li metal(20 mAh) cell with >10-fold Li excess capacity in commercial carbonate electrolyte (1 M $LiPF_6$ in ethylene carbonate/dimethyl carbonate [DMC], weight ratio of 1:1) (Figure S10). The much better performance of NMC 811(2 mAh)||Li_xSi(2 mAh) cell in commercial electrolytes demonstrates the critical role of that Li_xSi host on Li plating/stripping. The high energy density (600 Wh/kg), 300 cycle lifetime, and high rate capability of the NMC 811(2 mAh)||Li_xSi(2 mAh) cell make it very attractive for electric vehicle applications. Moreover, the all-fluorinated electrolyte applied here is non-flammable,[36] which can resolve safety issues. Here, it needs to be mentioned that the NMC 811(2 mAh)||Li_xSi(2 mAh) battery is different from the NMC 811(2 mAh)||Si(1.0 mAh) normal battery with Li plating on the Si anode, where the low CE of Si and Li plating on Si cause rapid capacity decay at a rate much faster than the NMC 811(2 mAh)||Si(2.0 mAh) battery (Figures 6C, 6D, and S7B).

EXPERIMENTAL PROCEDURES

Electrode Preparation and Electrochemical Measurements

The cathode NMC 811 electrode laminates (~10 mg active material and 2 mAh cm^{-2}) were supplied by Argon National Lab.

To prepare the silicon electrode, silicon was mixed with carbon black and LiPAA (lithium polyacrylate) binder with a mass ratio 80:10:10 into a homogeneous slurry in water with a pestle and mortar. The slurry mixture was coated onto a Cu foil and then dried at 100°C for 12 hr. The loading mass of the active materials for the electrode is about 2 mg/cm^2. The LiPAA binder was prepared by ion exchange according to a previous report,[37] neutralization being accomplished by the addition of equimolar amounts of LiOH to aqueous solutions of PAA for a final solution pH ≈ 7. PAA solutions were prepared from a 25 wt % solution in water (≈ molecular weight of 240,000, Alfa Aesar). The all-fluorinated electrolyte solution comprised of 1 M $LiPF_6$ in FEC/ FDEC/HFE (2:6:2 by volume). The cells were assembled with a polypropylene microporous film (Celgard 3501) as the separator. The electrochemical tests were performed using a coin-type cell (CR2016), which is fabricated in a glove box filled with Argon. Electrochemical performance was tested using an Arbin battery test station (BT2000, Arbin Instruments, USA).

SEM and TEM

The morphologies of the samples were examined using a Hitachi SU-70 field emission SEM and a JEOL 2100F field emission TEM.

XPS

The surface chemistry of the electrodes after cycling was examined by XPS using a Kratos AXIS 165 spectrometer. The electrodes were then taken out from the cell after cycles, and rinsed by DMC inside the glove box three times. All samples were dried under vacuum overnight, placed in a sealed bag, and then transferred into the XPS chamber under inert conditions in an Argon-filled glove bag. XPS data were collected using a monochromated Al Kα X-ray source (1,486.7 eV). The working pressure of the chamber was lower than 6.6×10^{-9} Pa. All reported binding energy values are calibrated to the C1s peak at 284.8 eV.

In Situ *Observation Cell*

The *in situ* observation cell (illustrated in Figure S9B) was homemade and fitted in the stage of an optical microscope (OMAX MD82ES10) (Figure S9A). Two stainless steel meshes, connected with two stainless steel rods, were applied as the current collector.

To provide an insight in the high CE at an atomic scale, two types of calculations were performed: (1) MD simulations using large-scale atomic/molecular massively (LAMMPS) code;[38] (2) first-principles calculation based on density function theory (DFT) using the Vienna Ab initio Simulation Package (VASP) package.[39]

MD Simulations

All the MD simulations were performed using the ReaxFF force field.[40,41] The structures of amorphous Li_xSi (x = 0.33, 1, 2.75, 3.25, 3.75, and 4.4) is modeled with a three-step process as in previous work. Firstly, the Li_xSi are heated to 2,000 K and then annealed for 100 ps. We then cooled the Li_xSi structures from 2,000 K to room temperature at a quenching rate of 0.085 K/fs to form an amorphous solid material with a 1-fs time step. Finally, a 100-ps equilibrium step at 300 K was performed to obtain the energies and PDF ($_g(r)$). The energies were calculated by averaging the total energy of the 100 ps and PDF is defined as

$$g(r) = \frac{V}{N}\frac{n(r)}{4\pi r^2 \Delta r},$$

where $n(r)$ represents particles in the shell within the region $r \pm \Delta r/2$, where Δr is the shell thickness and N demotes the number of particles in the model volume V.

To demonstrate the plating of lithium metal on the Li-Si alloy, we applied hybrid grand canonical Monte Carlo (MC)/MD simulations based on the Metropolis algorithm within the LAMMPS code. The possible MC moves include: (1) inserting a lithium atom into the system at a random position, (2) removing a random lithium atom from the system, and (3) moving a lithium atom to a new random position in the system. The Li chemical potential is calculated to be −35.3 kcal/mol using metallic Li. The temperature is controlled using a Berendsen thermostat.

DFT Calculations

First-principles computations based on DFT[42,43] are performed using the VASP. The projector augmented-wave method[44] with an energy cutoff of 520 eV is used to describe the ion-electron interaction on a well-converged k-point mesh. The Perdew-Burke-Ernzerhof functional in the generalized gradient approximation[45] is employed to calculate the exchange-correlation energy. The geometry optimizations

are performed using the conjugated gradient method, and the convergence threshold is set to be 10^{-5} eV in energy and 0.01 eV/Å in force. The binding energy and different charge density is calculated by subtracting the free energy and charge density of the substrate and Li atom from the Li-absorbed system, respectively.

SUPPLEMENTAL INFORMATION

Supplemental Information includes ten figures and two videos and can be found with this article online at https://doi.org/10.1016/j.joule.2018.11.025.

ACKNOWLEDGMENTS

This work was supported by the US Department of Energy (DOE) under award nos. DEEE0008200 and DEEE0008202. The support of the Maryland NanoCenter and its AIM Lab is acknowledged. The electrodes of NMC(811) were produced and provided by Argonne National Laboratory.

AUTHOR CONTRIBUTIONS

L.C. and X.F. designed the experiments, analyzed data, and wrote the paper. L.C., X.F., J.C., and S.H. conducted the experiments. X.J. conducted the calculations. C.W. conceived and supervised the project. All authors contributed to interpretation of the results.

DECLARATION OF INTERESTS

The authors declare no competing interests.

Received: October 1, 2018
Revised: November 16, 2018
Accepted: November 29, 2018
Published: December 21, 2018

REFERENCES

1. Dunn, B., Kamath, H., and Tarascon, J.M. (2011). Electrical energy storage for the grid: a battery of choices. Science *334*, 928–935.
2. Goodenough, J.B., and Park, K.S. (2013). The Li-ion rechargeable battery: a perspective. J. Am. Chem. Soc. *135*, 1167–1176.
3. Tarascon, J.-M., and Armand, M. (2001). Issues and challenges facing rechargeable lithium batteries. Nature *414*, 359–367.
4. Lin, D., Liu, Y., and Cui, Y. (2017). Reviving the lithium metal anode for high-energy batteries. Nat. Nanotech. *12*, 194–206.
5. Xu, W., Wang, J., Ding, F., Chen, X., Nasybulin, E., Zhang, Y., and Zhang, J. (2014). Lithium metal anodes for rechargeable batteries. Energy Environ. Sci. *7*, 513–537.
6. Zheng, G., Lee, S.W., Liang, Z., Lee, H.W., Yan, K., Yao, H., Wang, H., Li, W., Chu, S., and Cui, Y. (2014). Interconnected hollow carbon nanospheres for stable lithium metal anodes. Nat. Nanotech. *9*, 618–623.
7. Qian, J., Henderson, W.A., Xu, W., Bhattacharya, P., Engelhard, M., Borodin, O., and Zhang, J.G. (2015). High rate and stable cycling of lithium metal anode. Nat. Commun. *6*, 6362–6370.
8. Zheng, J., Engelhard, M.H., Mei, D., Jiao, S., Polzin, B.J., Zhang, J., and Xu, W. (2017). Electrolyte additive enabled fast charging and stable cycling lithium metal batteries. Nat. Energy *2*, 17012.
9. Bhattacharyya, R., Key, B., Chen, H., Best, A.S., Hollenkamp, A.F., and Grey, C.P. (2010). In situ NMR observation of the formation of metallic lithium microstructures in lithium batteries. Nat. Mater. *9*, 504–510.
10. Chandrashekar, S., Trease, N.M., Chang, H.J., Du, L.S., Grey, C.P., and Jerschow, A. (2012). ^{7}Li MRI of Li batteries reveals location of microstructural lithium. Nat. Mater. *11*, 311–315.
11. Harry, K.J., Hallinan, D.T., Parkinson, D.Y., MacDowell, A.A., and Balsara, N.P. (2013). Detection of subsurface structures underneath dendrites formed on cycled lithium metal electrodes. Nat. Mater. *13*, 69–73.
12. Liang, X., Pang, Q., Kochetkov, I.R., Sempere, M.S., Huang, H., Sun, X., and Nazar, L.F. (2017). A facile surface chemistry route to a stabilized lithium metal anode. Nat. Energy *2*, 17119.
13. Ding, F., Xu, W., Graff, G.L., Zhang, J., Sushko, M.L., Chen, X., Shao, Y., Engelhard, M.H., Nie, Z., Xiao, J., et al. (2013). Dendrite-free lithium deposition via self-healing electrostatic shield mechanism. J. Am. Chem. Soc. *135*, 4450–4456.
14. Liu, K., Pei, A., Lee, H.R., Kong, B., Liu, N., Lin, D., Liu, Y., Liu, C., Hsu, P.C., Bao, Z., and Cui, Y. (2017). Lithium metal anodes with an adaptive "solid-liquid" interfacial protective layer. J. Am. Chem. Soc. *139*, 4815–4820.
15. Zheng, J., Yan, P., Mei, D., Engelhard, M.H., Cartmell, S.S., Polzin, B.J., Wang, C., Zhang, J., and Xu, W. (2016). Highly stable operation of lithium metal batteries enabled by the formation of a transient high-concentration electrolyte layer. Adv. Energy Mater. *6*, 1502151.
16. Lin, D., Liu, Y., Liang, Z., Lee, H.W., Sun, J., Wang, H., Yan, K., Xie, J., and Cui, Y. (2016). Layered reduced graphene oxide with nanoscale interlayer gaps as a stable host for lithium metal anodes. Nat. Nanotech. *11*, 626–632.
17. Yan, K., Lu, Z., Lee, H., Xiong, F., Hsu, P., Li, Y., Zhao, J., Chu, S., and Cui, Y. (2016). Selective deposition and stable encapsulation of lithium through heterogeneous seeded growth. Nat. Energy *1*, 16010.
18. Liu, L., Yin, Y., Li, J., Li, N., Zeng, X., Ye, H., Guo, Y., and Wan, L. (2017). Free-standing hollow

carbon fibers as high-capacity containers for stable lithium metal anodes. Joule *1*, 1–13.

19. Wang, T., Salvatierra, R.V., Jalilov, A.S., Tian, J., and Tour, J.M. (2017). Ultrafast charging high capacity asphalt-lithium metal batteries. ACS Nano *11*, 10761–10767.

20. Liu, Y., Lin, D., Liang, Z., Zhao, J., Yan, K., and Cui, Y. (2016). Lithium-coated polymeric matrix as a minimum volume-change and dendrite-free lithium metal anode. Nat. Commun. *7*, 10992.

21. Liang, Z., Lin, D., Zhao, J., Lu, Z., Liu, Y., Liu, C., Lu, Y., Wang, H., Yan, K., Tao, X., and Cui, Y. (2016). Composite lithium metal anode by melt infusion of lithium into a 3D conducting scaffold with lithiophilic coating. Proc. Natl. Acad. Sci. U S A *113*, 2862–2867.

22. Lu, L.L., Ge, J., Yang, J.N., Chen, S.M., Yao, H.B., Zhou, F., and Yu, S.H. (2016). Free-standing copper nanowire network current collector for improving lithium anode performance. Nano Lett. *16*, 4431–4437.

23. Noh, M., Kwon, Y., Lee, H., Cho, J., Kim, Y., and Kim, M. (2005). Amorphous carbon-coated tin anode material for lithium secondary battery. Chem. Mater. *17*, 1926–1929.

24. Tang, W., Yin, X., Kang, S., Chen, Z., Tian, B., Teo, S.L., Wang, X., Chi, X., Loh, K.P., Lee, H.W., and Zheng, G.W. (2018). Lithium silicide surface enrichment: a solution to lithium metal battery. Adv. Mater. e1801745, https://doi.org/10.1002/adma.201801745.

25. Tu, Z., Choudhury, S., Zachman, M.J., Wei, S., Zhang, K., Kourkoutis, L.F., and Archer, L.A. (2018). Fast ion transport at solid-solid interfaces in hybrid battery anodes. Nat. Energy *3*, 310–316.

26. Chan, C.K., Peng, H., Liu, G., McIlwrath, K., Zhang, X.F., Huggins, R.A., and Cui, Y. (2008). High-performance lithium battery anodes using silicon nanowires. Nat. Nanotech. *3*, 31–35.

27. Kovalenko, I., Zdyrko, B., Magasinski, A., Hertzberg, B., Milicev, Z., Burtovyy, R., Luzinov, I., and Yushin, G. (2011). A major constituent of brown algae for use in high-capacity Li-ion batteries. Science *334*, 75–79.

28. Choi, S., Kwon, T., Coskun, A., and Choi, J.W. (2017). Highly elastic binders integrating polyrotaxanes for silicon microparticle anodes in lithium ion batteries. Science *357*, 279–283.

29. Markevich, E., Salitra, G., and Aurbach, D. (2017). Fluoroethylene carbonate as an important component for the formation of an effective solid electrolyte interphase on anodes and cathodes for advanced Li-ion batteries. ACS Energy Lett. *2*, 1337–1345.

30. Fan, X., Chen, L., Borodin, O., Ji, X., Chen, J., Hou, S., Deng, T., Zheng, J., Yang, C., Liou, S.C., et al. (2018). Non-flammable electrolyte enables Li-metal batteries with aggressive cathode chemistries. Nat. Nanotech. *13*, 715–722.

31. Zhang, Q., Pan, J., Lu, P., Liu, Z., Verbrugge, M.W., Sheldon, B.W., Cheng, Y.T., Qi, Y., and Xiao, X. (2016). Synergetic effects of inorganic components in solid electrolyte interphase on high cycle efficiency of lithium ion batteries. Nano Lett. *16*, 2011–2016.

32. Lu, Y., Tu, Z., and Archer, L.A. (2014). Stable lithium electrodeposition in liquid and nanoporous solid electrolytes. Nat. Mater. *13*, 961–969.

33. Xu, C., Lindgren, F., Philipp, B., Gorgoi, M., Björefors, F., Edström, K., and Gustafsson, T. (2015). Improved performance of the silicon anode for Li-ion batteries: understanding the surface modification mechanism of fluoroethylene carbonate as an effective electrolyte additive. Chem. Mater. *27*, 2591–2599.

34. Wang, W., and Yang, S. (2017). Enhanced overall electrochemical performance of silicon/carbon anode for lithium-ion batteries using fluoroethylene carbonate as an electrolyte additive. J. Alloys Compd. *695*, 3249–3255.

35. Li, J., and Dahn, J.R. (2007). An in situ X-ray diffraction study of the reaction of Li with crystalline Si. J. Electrochem. Soc. *154*, A156–A161.

36. Hu, L., Zhang, Z., and Amine, K. (2013). Fluorinated electrolytes for Li-ion battery: an FEC-based electrolyte for high voltage $LiNi_{0.5}Mn_{1.5}O_4$/graphite couple. Electrochem. Commun. *35*, 76–79.

37. Pieczonka, N.P.W., Borgel, V., Ziv, B., Leifer, N., Dargel, V., Aurbach, D., Kim, J.H., Liu, Z., Huang, X., and Krachkovskiy, S.A. (2015). Lithium polyacrylate (LiPAA) as an advanced binder and a passivating agent for high-voltage Li-ion batteries. Adv. Energy Mater. *5*, 1501008.

38. Plimpton, S., Crozier, P., and Thompson, A. (2007). LAMMPS-Large-Scale Atomic/Molecular Massively Parallel Simulator, *18* (Sandia National Laboratories), p. 43.

39. Kresse, G., and Hafner, J. (1994). Ab initiomolecular-dynamics simulation of the liquid-metal-amorphous-semiconductor transition in germanium. Phys. Rev. B *49*, 14251–14269.

40. Ostadhossein, A., Cubuk, E.D., Tritsaris, G.A., Kaxiras, E., Zhang, S., and van Duin, A.C. (2015). Stress effects on the initial lithiation of crystalline silicon nanowires: reactive molecular dynamics simulations using ReaxFF. Phys. Chem. Chem. Phys. *17*, 3832–3840.

41. Van Duin, A.C., Dasgupta, S., Lorant, F., and Goddard, W.A. (2001). ReaxFF: a reactive force field for hydrocarbons. J. Phys. Chem. A *105*, 9396–9409.

42. Hohenberg, P., and Kohn, W. (1964). Inhomogeneous electron gas. Phys. Rev. *136*, B864.

43. Kohn, W., and Sham, L.J. (1965). Self-consistent equations including exchange and correlation effects. Phys. Rev. *140*, A1133.

44. Blöchl, P.E. (1994). Projector augmented-wave method. Phys. Rev. B *50*, 17953.

45. Perdew, J.P., Burke, K., and Ernzerhof, M. (1996). Generalized gradient approximation made simple. Phys. Rev. Lett. *77*, 3865.

JOUL, Volume *3*

Supplemental Information

High-Energy Li Metal Battery with Lithiated Host

Long Chen, Xiulin Fan, Xiao Ji, Ji Chen, Singyuk Hou, and Chunsheng Wang

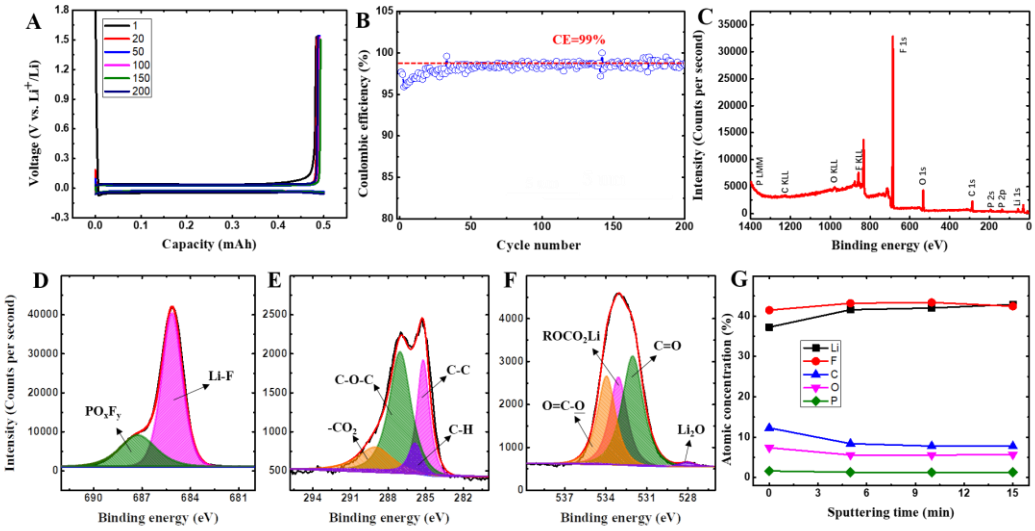

Figure S1 | Electrochemical performance of Li metal anode and XPS spectra of Li metal after cycled. (**A**) Galvanostatic charge-discharge profiles for the Li metal plating/stripping on a Cu working electrode cycled at a current density of 0.5 mA cm^{-2}; (**B**) Coulombic efficiency for the Li plating/stripping cycled at the current of 0.5 mA cm^{-2}; (**C**) Full XPS spectra of Li metal anode after 100 cycles at the current density of 0.5 mA cm^{-2} (without sputtering); (**D**) XPS spectra of F 1s for Li metal anode after 100 cycles (without sputtering); (**E**) XPS spectra of C 1s for Li metal anode after 100 cycles (without sputtering); (**F**) XPS spectra of O 1s for Li metal anode after 100 cycles (without sputtering); (**G**) Composition of the SEI after various duration of Ar^+ sputtering on the Li metal anode after 100 cycles.

The galvanostatic charge-discharge profiles show a small over-potential of about 60 mV and long cycling stability at the current density of 0.5 mA cm^{-2} (**Figure S1A**). The CE for Li plating/stripping was calculated from the capacity ratio of Li stripped from Cu after its deposition in the previous cycle. The CE for Li

plating/stripping reaches to ~99% (**Figure S1B**), which is much higher than that (~80%) in the conventional diluted electrolyte (i.e., Li salt concentration below 2.0 M)[1]. The composition of SEI on Li metal after 100 cycles in the all fluorinated electrolyte was characterized using X-ray photoelectron spectroscopy (XPS) (**Figure S1C-G**). The F 1s XPS spectra exhibit a relative high peak at 685.0 eV corresponding to Li-F bind (**Figure S1D**). In C1s spectra, carbonyl species at ~289.0 eV, ethereal carbon at ~ 287.0 eV, and hydrocarbon at ~285.0 eV were detected for the SEI (**Figure S1E**), along with C=O, O=C-O, $ROCO_2Li$, and Li_2O species in the O1s spectra (**Figure S1F**). However, according to the atomic concentration (at. %) of elements among the SEI composition, the most elements are Lithium (Li) 37.24% and fluorine (F) 41.45% (without sputtering), moreover, with the increase of sputtering time, the contents of Li and F increase, which indicate the extremely high content of Lithium fluoride (LiF). We believed that, they originated from the reduction of fluorinated solvent in the all fluorinated electrolyte. LiF is a good electronic insulator that can block the electron leakage through the SEI, therefore prevent the continuous electrolyte consumption[2], in addition, LiF is also known to exhibit a high interfacial energy to Li metal[3], which facilitates Li^+ transport along the interface and promotes the growth of the deposited Li metal in parallel rather than vertical direction with regard to the Li-metal plane. These features further reduce the specific surface area, minimize the side-reactions, and suppress the onset of dendritic growth.

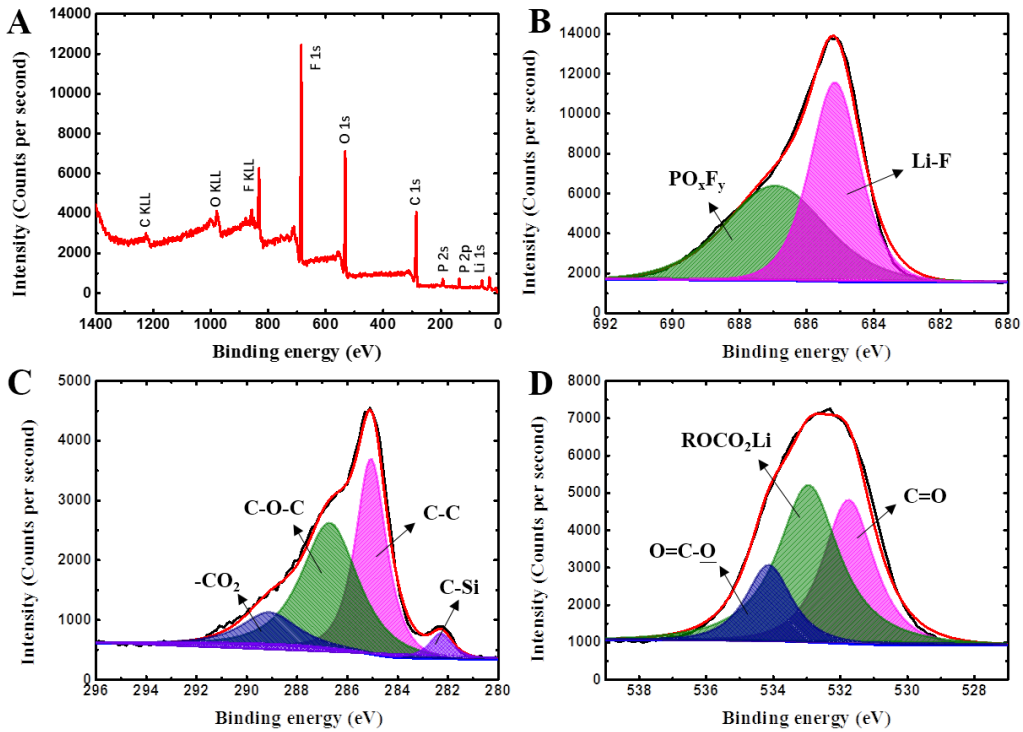

Figure S2 | XPS results of silicon electrode after cycles. (A) Full XPS spectra of silicon electrode after 100 cycles at the current density of 0.5mA cm^{-1} between 0.005-1.5V in all fluorinated electrolyte (1M $LiPF_6$ in FEC/FDEC/HFE) (without sputtering). (**B**) XPS spectra of **F 1s** for silicon electrode after 100 cycles in all fluorinated electrolyte (without sputtering); (**C**) XPS spectra of **C 1s** for silicon electrode after 100 cycles in all fluorinated electrolyte (without sputtering); (**D**) XPS spectra of **O 1s** for silicon electrode after 100 cycles in all fluorinated electrolyte (without sputtering).

X-ray photoelectron spectroscopy (XPS) was employed to investigate the components of the SEI generated on cycled silicon electrode. As seen in the F 1s XPS spectra in **Figure S2B**, the peak intensity mostly can be assigned to LiF at 685.0 eV. The LiF based SEI may be mainly produced from the decomposition of fluorinated slovents (FEC, FDEC, HFE). LiF is a good electric insulator thereby blocking the electron

leakage through the SEI layer, which can prevent the additional electrolyte decomposition. In C1s spectra, carbonyl species at ~289.0 eV, ethereal carbon at ~ 287.0 eV, and carbon-carbon at ~285.0 eV were detected for the SEI (**Figure S2C**), in addition we also observed a peak at ~282.5 eV that can be assigned to C-Si bind, which originated from the Si alloy material[4]. The C=O, O=C-O, $ROCO_2Li$, and Li_2O species were also detected in the O1s spectra (**Figure S2D**).

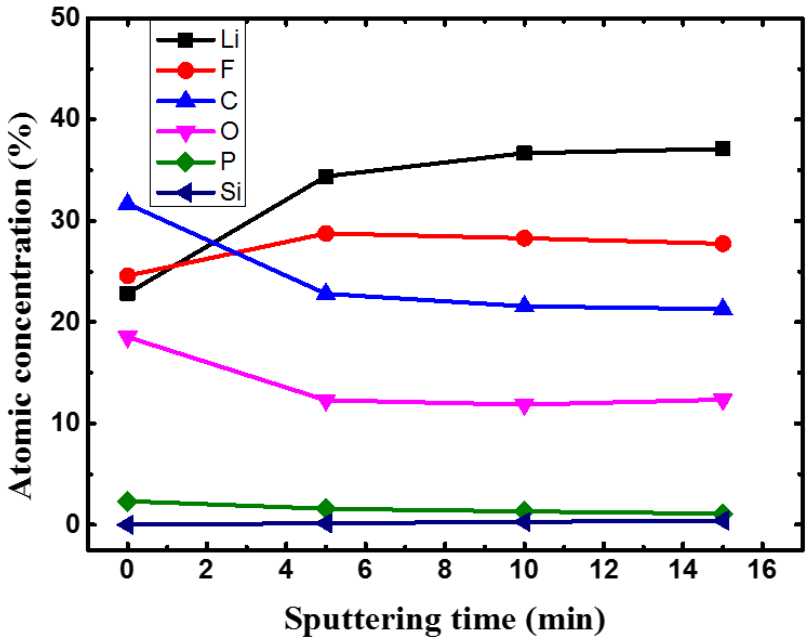

Figure S3 | Composition of the SEI after various duration of Ar^+ sputtering on the Si anode after 100 cycles. According to the atomic concentration (at. %) of elements among the SEI composition, the most elements are Lithium (Li) 37% and fluorine (F) 28% (after 15mins sputtering), which indicate the extremely high content of Lithium fluoride (LiF).

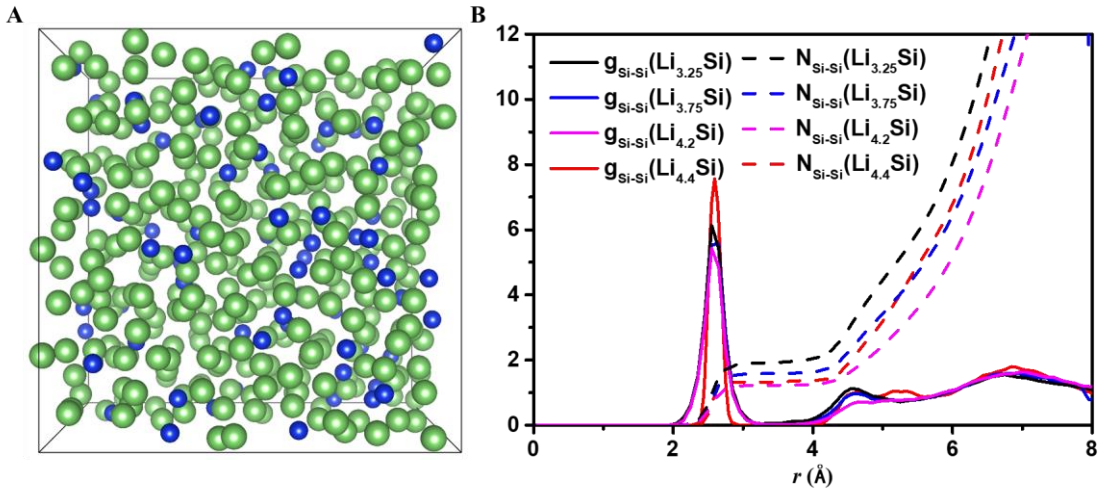

Figure S4 | the (A) typical structure and (B) PDF for Si-Si pairs in $Li_{3.75\pm w}Si$ alloys. No sharp second-neighbor peak is present in the PDF of Li3.75±wSi alloys, which confirms the amorphous nature of the Li-Si alloy. The PDF exhibits a distinct peak at 2.5 Å indicating the average distance of seeds for Li nucleation.

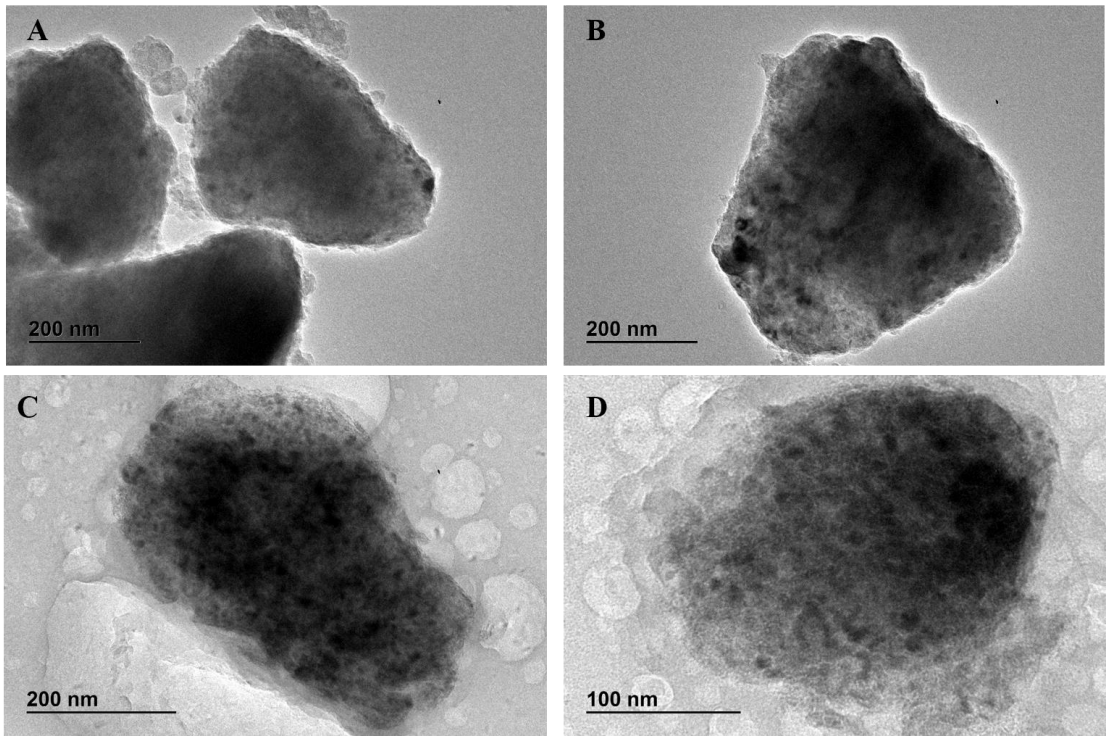

Figure S5 | TEM images of the fresh Si and Si after Li plating and stripping process. (**A-B**) TEM images of fresh Si; (**C-D**) TEM images of the Si after Li plating and stripping process.

The Si after Li plating and stripping process was achieved by discharging the electrode discharged to 0.005V at the current of 0.5 mA cm^{-2} and continue discharging with a capacity of 2mAh at the current of 0.5 mA cm^{-2}, than charging 2 mAh at the current of 0.5 mA cm^{-2}. Compared to the fresh Si TEM images, it is obvious that, the surface area of Si after Li plating and stripping process emerge some nano pores.

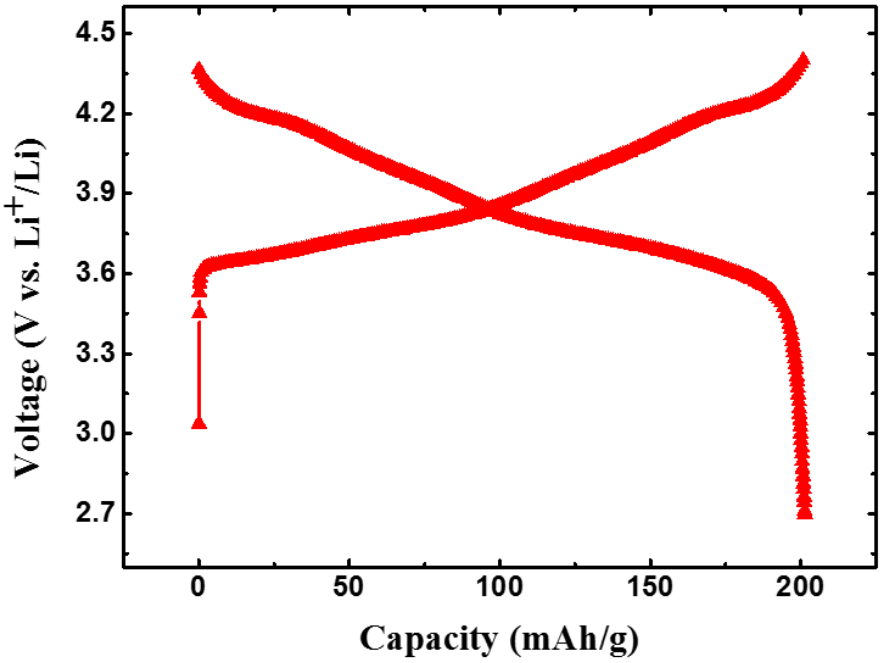

Figure S6 | Galvanostatic charge-discharge profiles of NMC811. Galvanostatic charge-discharge profiles of NMC811 at the current density of 0.5 mA cm^{-2} between 2.7-4.4V in all fluorinated electrolyte.

The NMC811 cathode delivered a specific capacity of 200 mAh g^{-1}, the coulombic efffciency is above 99.99%, with a high area capacity of ~2 mAh cm^{-2}.

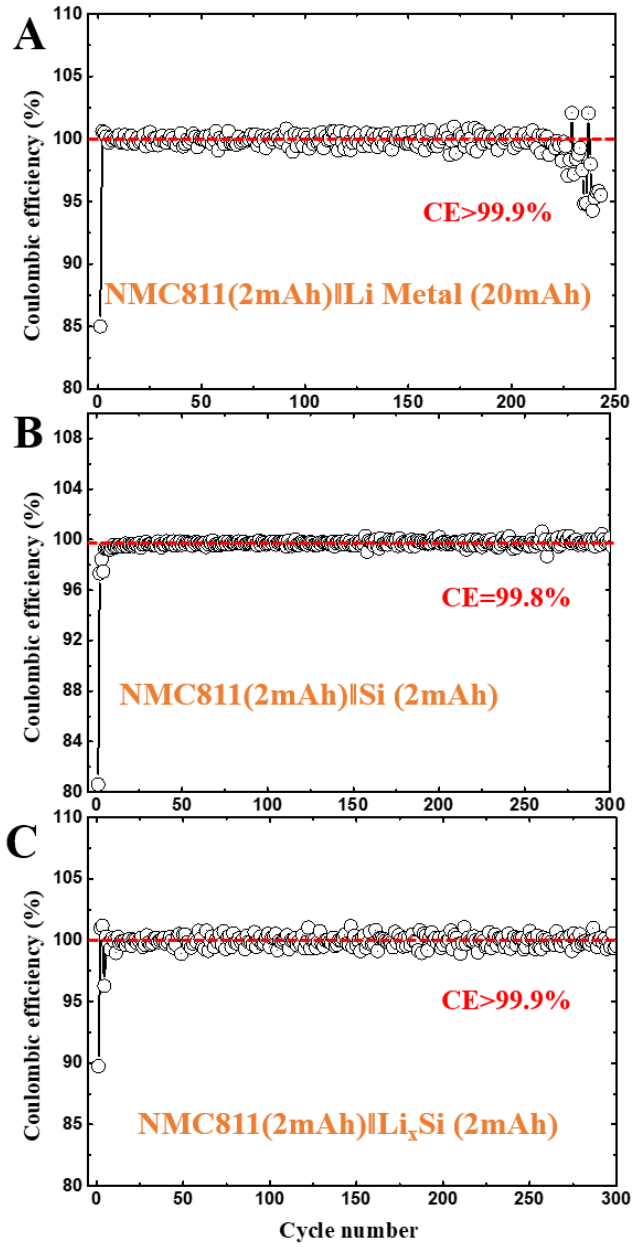

Figure S7 | Coulombic efficiency of batteries using NMC811 cathode with different anodes. (**A**) Coulombic efficiency of NMC811(2 mAh)||Li metal(20 mAh) battery at the current density of 0.5 mA cm^{-2} between 2.7-4.4V; (**B**) Coulombic efficiency of NMC811(2 mAh)||Si(2 mAh) battery at the current density of 0.5 mA cm^{-2} between 1.8-4.4V; (**C**) Coulombic efficiency of NMC811(2 mAh)||Li_xSi(2 mAh) battery at the current density of 0.5 mA cm^{-2} between 1.8-4.4V.

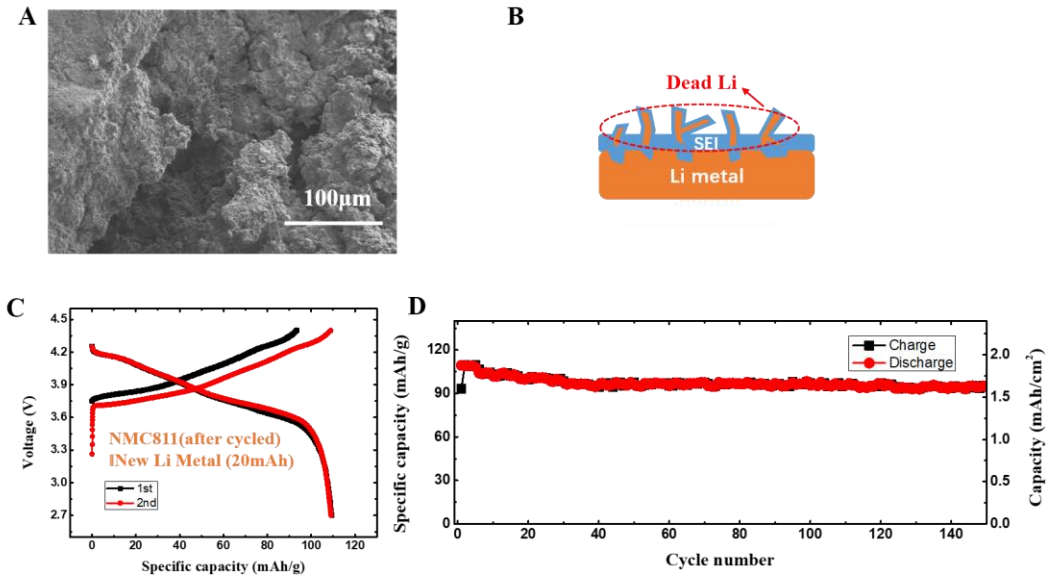

Figure S8 | SEM images of Li anode after 240 cycles (half capacity lost) in NMC811(2 mAh)||Li metal(20 mAh) battery and Electrochemical performances of LMB battery using the same NMC811 electrode and a new Li metal anode (200 mAh).

(**A**) SEM images of Li anode after 240 cycles (half capacity lost) in NMC811(2 mAh)||Li metal(20 mAh) battery; (**B**) Schematic diagrams of dead Li on the Li metal anode; (**C**) Galvanostatic charge-discharge profiles of LMB battery with the same NMC811 electrode and a new Li metal anode at the current density of 0.5 mA cm^{-2} between 2.7-4.4V; (**D**) Cycle performance of LMB battery with the same NMC811 electrode and a new Li metal anode at the current density of 0.5 mA cm^{-2} between 2.7-4.4V.

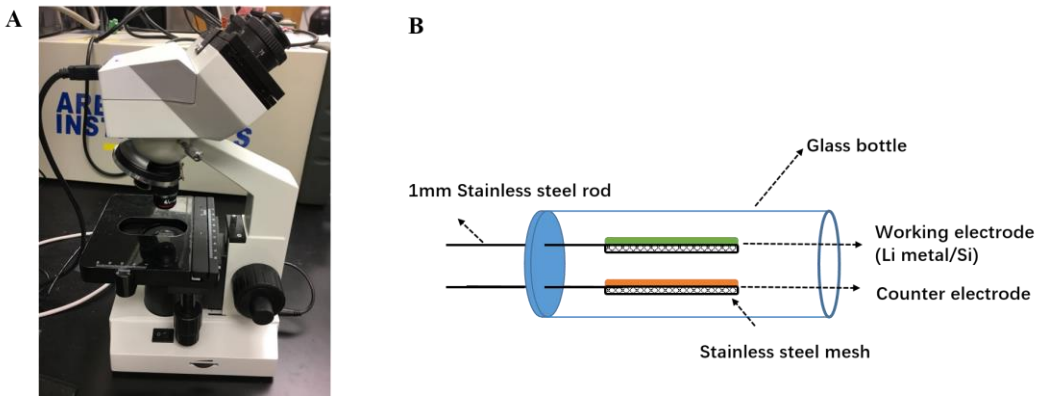

Figure S9 | In situ observation cell and optical microscope: (**A**) the optical microscope (OMAX MD82ES10); (**B**) the visualization setup for in situ optical microscope observation of the electrodeposition.

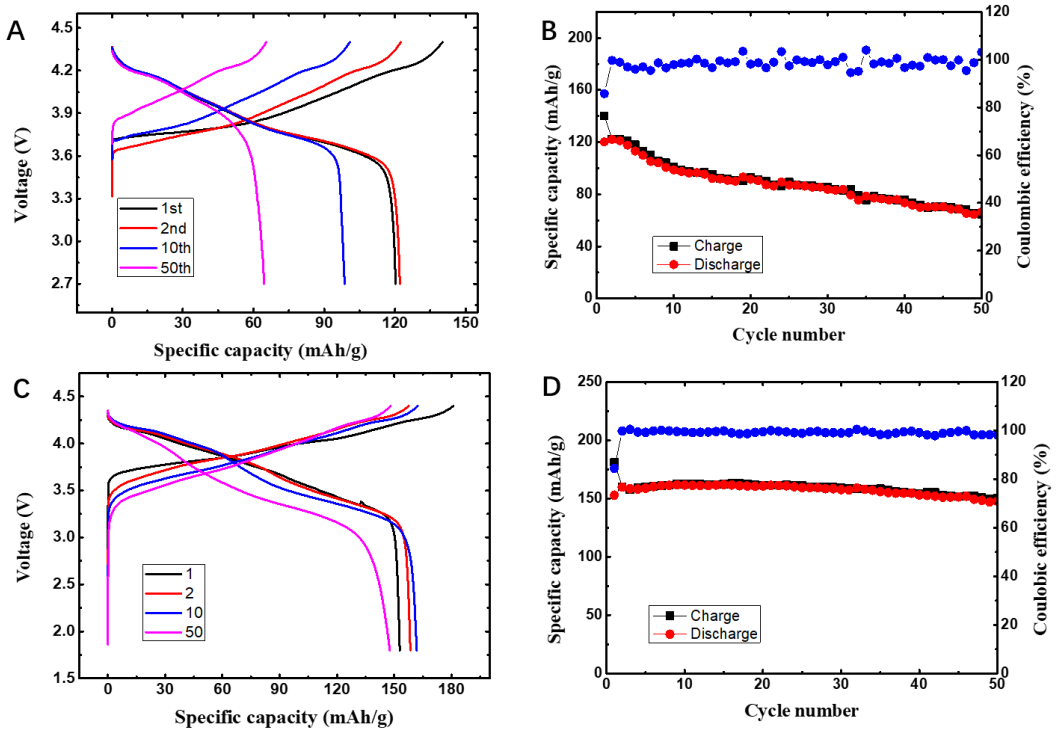

Figure S10 | Electrochemical performances of NMC811/Li and NMC811/LixSi cells in commercial electrolyte (1M $LiPF_6$ in EC/DMC). (**A**) Galvanostatic charge-discharge profiles of NMC811(2 mAh)||Li metal(20 mAh) battery at the current density of 0.5 mA cm^{-2} between 2.7-4.4V, the weight of 2 mAh NMC811 is ~10 mg and 20 mAh Li metal is ~5.5 mg; (B) Cycle performance of NMC811(2 mAh)||Li metal(20 mAh) battery at the current density of 0.5 mA cm^{-2} between 2.7-4.4V; (C) Galvanostatic charge-discharge profiles of NMC811(2 mAh)||Li_xSi(2 mAh) battery at the current density of 0.5 mA cm^{-2} between 1.8-4.4V, the weight of 2 mAh Li_xSi is ~2.5 mg; (D) Cycle performance of NMC811(2 mAh)||Li_xSi (2 mAh) battery at the current density of 0.5 mA cm^{-2} between 1.8-4.4V

We fabricated and compared the cycle performance of NMC811(2mAh)||Li metal (20mAh) cell and NMC NMC811(2 mAh)||LixSi(2 mAh) cell with the regular carbonate electrolyte (1 M $LiPF_6$ in EC/DMC, weight ratio of 1:1). **Figure S10** shows

that the capacity of NMC811(2 mAh)||Li metal(20 mAh) cell in 1 M $LiPF_6$ in EC/DMC rapidly decreases to 50% after 50 cycles even excess Li anode (~5mg, 20 mAh) with 10 times more capacities is used. In addition, Coulombic efficiency of less than 97% is also very low. The poor performance of NMC811(2 mAh)||Li metal(20 mAh) cell in 1 M $LiPF_6$ in EC/DMC electrolyte is mainly attributed to Li dendrite growth and formation of dead Li during charge/discharge cycles in the EC/DMC electrolyte. In sharp contrast, the NMC811(2 mAh)||Li_xSi (2 mAh) cell maintains more than 90% after 50 cycles in the regular EC/DMC based electrolytes even with only one fold Li excess. The Coulombic efficiency is stable and around 100%, which indicate the stable and high Coulombic efficiency of Li metal plating/stripping on the Li_xSi host.

Reference

1. Qian, J., *et al.* (2015) High rate and stable cycling of lithium metal anode. *Nat. Commun.* **6**, 6362.

2. Zhang, Q. *et al.* (2016) Synergetic Effects of Inorganic Components in Solid Electrolyte Interphase on High Cycle Efficiency of Lithium Ion Batteries. *Nano Lett.* **16**, 2011-2016.

3. Lu, Y., Tu, Z., Archer, L. A. (2014) Stable lithium electrodeposition in liquid and nanoporous solid electrolytes. *Nature Mater*. **13**, 961-969.

4. Contarini, S., Howlett, S. P., Rizzo, C., and De Angelis, B. A. (1991) XPS study on the dispersion of carbon additives in silicon carbide powders. *Applied Surface Scienc*e **51**, 177-183.